Journal of Turbomachinery Published by ASME

Dear Author,

Congratulations on having your paper accepted for publication in the ASME Journal Program.

Your page proof is available in PDF format from the ASME Proof Download & Corrections site here:

http://115.111.50.156/jw/AuthorProofLogin.aspx?pwd=c8ce9219091a

Login: your e-mail address

Password: c8ce9219091a

Please keep this email in case you need to refer back to it in the future.

You will need Adobe Acrobat Reader software to view the file. This is free software and a download link is provided when you log in to view your proofs.

Responsibility of detecting errors rests with the author. Please review the page proofs carefully and:

1) Answer any queries on the first page "Author Query Form"

2) Proofread any tables and equations carefully

3) Check to see that any special characters have translated correctly

RETURNING CORRECTIONS:

To return corrections, please use the ASME Proof Download & Corrections Submission Site (link above) and provide either:

1. Annotated PDF

2. Text entry of corrections, with line numbers, in the text box provided

Additional files, as necessary, can also be uploaded through the site.

SPECIAL NOTES:

Your Login and Password are valid for a limited time. Please reply within 48 hours. Your prompt attention to and return of page proofs will speed the publication of your work.

For all correspondence, please include your article no. (TURBO-12-1136) in the subject line.

This e-proof is to be used only for the purpose of returning corrections to the publisher.

If you have any questions, please contact: asme.cenveo@cenveo.com.

Sincerely,

Isabel Castillo, Journal Production Manager

STATEMENT OF EDITORIAL POLICY AND PRACTICE

The Technical Committee on Publications and Communications (TCPC) of ASME aims to maintain a high degree of technical, literary, and typographical excellence in its publications. Primary consideration in conducting the publications is therefore given to the interests of the reader and to safeguarding the prestige of the Society.

To this end the TCPC confidently expects that sponsor groups will subject every paper recommended by them for publication to careful and critical review for the purpose of eliminating and correcting errors and suggesting ways in which the paper may be improved as to clarity and conciseness of expression, accuracy of statement, and omission of unnecessary and irrelevant material. The primary responsibility for the technical quality of the papers rests with the sponsor groups.

In approving a paper for publication, however, the TCPC reserves the right to submit it for further review to competent critics of its own choosing if it feels that this additional precaution is desirable. The TCPC also reserves the right to request revision or condensation of a paper by the author or by the staff for approval by the author. It reserves the right, and charges the editorial staff, to eliminate or modify statements in the paper that appear to be not in good taste and hence likely to offend readers (such as obvious advertising of commercial ventures and products, comments on the intentions, character, or acts of persons and organizations that may be construed as offensive or libelous), and to suggest to authors rephrasing of sentences where this will be in the interest of clarity. Such rephrasing is kept to a minimum.

Inasmuch as specific criteria for the judging of individual cases cannot, in the opinion of the TCPC, be set up in any but the most general rules, the TCPC relies upon the editorial staff to exercise its judgment in making changes in manuscripts, in rearranging and condensing papers, and in making suggestions to authors. The TCPC realizes that the opinions of author and editor may sometimes differ, and hence it is an invariable practice that no paper is published until it has been passed on by the author. For this purpose page proofs of the edited paper are sent to the author prior to publication in a journal. Changes in content and form made in the proofs by authors are followed by the editor except in cases in which the Society's standard spelling and abbreviation forms are affected.

If important differences of opinion arise between author and editor, the points at issue are discussed in correspondence or interview, and if a solution satisfactory to both author and editor is not reached, the matter is laid before the TCPC for adjustment.

Technical Committee on Publications and Communications (TCPC)
Reviewed: 05/2012

AUTHOR QUERY FORM

ASME — SETTING THE STANDARD	**Journal: J. Turbomach.** **Article Number: TURBO-12-1136**	**Please provide your responses and any corrections by** **annotating this PDF and uploading it to ASME's eProof** **website as detailed in the Welcome email.**

Dear Author,

Below are the queries associated with your article; please answer all of these queries before sending the proof back to Cenveo. Production and publication of your paper will continue after you return corrections or respond that there are no additional corrections.

Location in article	Query / Remark: click on the Q link to navigate to the appropriate spot in the proof. There, insert your comments as a PDF annotation.
AQ1	The abstract should be a single paragraph and has been edited accordingly. Please review.
AQ2	The abstract must be self-contained, i.e., no reference citations. Please review the reference information added in place of the citation.
AQ3	In the sentence beginning "numerical simulations with," please define "MISES."
AQ4	Please confirm reference citation in Table 2.
AQ5	In the sentence beginning, "the shape factor is calculated," please define "IMR."
AQ6	Please provide page numbers for Ref. 2.
AQ7	Please confirm definition of "FEDSM" in Ref. 5.
AQ8	Please confirm definition of "IMECE" in Ref. 6
AQ9	Please provide page numbers for Ref. 13.
AQ10	Please confirm the definition of "ICALEO" in Ref. 15.
AQ11	Please define "IGTC" in Ref. 19.

Thank you for your assistance.

Christoph Lietmeyer
Test Engineer
Volkswagen AG,
38436 Wolfsburg, Germany
e-mail: Christoph.Lietmeyer@volkswagen.de

Berend Denkena
Professor
Institute of Production Engineering
and Machine Tools,
Leibniz Universitaet Hannover,
30823 Garbsen, Germany
e-mail: Denkena@ifw.uni-hannover.de

Rainer Kling
Business Unit Manager Laser Micromachining,
Centre Technologique ALPhANOV,
351 Cours de la Libération,
33405 Talence, France
e-mail: rainer.kling@alphanov.com

Thomas Krawczyk
Research Assistant
Institute of Production Engineering
and Machine Tools,
Leibniz Universitaet Hannover,
30823 Garbsen, Germany
e-mail: krawczyk@ifw.uni-hannover.de

Ludger Overmeyer
Professor
Laser Zentrum Hannover e.V.,
Hollerithallee 8,
30419 Hannover, Germany
e-mail: ludger.overmeyer@ita.uni-hannover.de

Eduard Reithmeier
Professor
e-mail: sekretariat@imr.uni-hannover.de

Renke Scheuer
Research Assistant
e-mail: renke.scheuer@imr.uni-hannover.de

Taras Vynnyk
Group Leader Industrial and Medical Imaging
e-mail: taras.vynnyk@imr.uni-hannover.de

Institute of Measurement and Automatic Control,
Leibniz Universitaet Hannover,
Nienburger Str. 17,
30167 Hannover, Germany

Bodo Wojakowski
Research Assistant
Laser Zentrum Hannover e.V.,
Hollerithallee 8,
30419 Hannover, Germany
e-mail: b.wojakowski@lzh.de

Recent Advances in Manufacturing of Riblets on Compressor Blades and Their Aerodynamic Impact

Since Oehlert et al. (2007, "Exploratory Experiments on Machined Riblets for 2-D Compressor Blades," Proceedings of International Mechanical Engineering Conference and Exposition 2007, Seattle, WA, IMECE 2007 – 43457.), significant improvements in the manufacturing processes of riblets by laser structuring and grinding have been achieved. In the present study, strategies for manufacturing small-scale grooves with a spacing smaller than 40 μm by metal bonded grinding wheels are presented. For the laser-structuring process, significant improvements of the production time by applying diffractive optical elements were achieved. Finally, strategies for evaluating the geometrical quality of the small-scale surface structures are shown and results obtained with two different measuring techniques (SEM and confocal microscope) are compared with each other. The aerodynamic impact of the different manufacturing processes is investigated based upon skin friction reduction data obtained on flat plates as well as the profile-loss reduction of riblet-structured compressor blades measured in a linear cascade wind tunnel. Numerical simulations with MISES embedded in a Monte Carlo simulation (MCS) were performed in order to calculate the profile-loss reduction of a blade structured by grinding to define further improvements of the riblet-geometry. A numerical as well as experimental study quantifying the relevant geometrical parameters indicate how further improvements from the present 4% reduction in skin friction can be achieved by an additional decrease of the riblet tip diameter and a more trapezoidal shape of the groove in order to realize the 8% potential reduction. [DOI: 10.1115/1.4007590]

Joerg R. Seume

Professor, Senior Member ASME
Institute of Turbomachinery and Fluid Dynamics,
Leibniz Universitaet Hannover,
30167 Hannover, Germany
e-mail: Seume@tfd.uni-hannover.de

Introduction

A major goal in turbomachinery design is the increase of efficiency in order to reduce the fuel consumption of aircraft engines or gas turbines and, hence, the operating costs and CO_2-emissions. To attain an increase of efficiency, the flow losses must be reduced. Approximately 50% of the losses are generated by the secondary flows (Gümmer [1]). Thus, approximately 50% of the losses are generated by the blading with a dominant portion of the friction losses, especially in the turbulent boundary layer of compressor blades with an early onset of boundary layer transition near the leading edges. Therefore, a decrease of skin friction leads to an additional increase in efficiency.

It is known that small ribs on the surface, oriented in the mean flow direction, can reduce skin friction in the case of turbulent boundary layer flow when their geometric properties are appropriate to the local flow conditions. These ribs, also known as riblets, are, therefore, a passive control mechanism to reduce drag and can also be found in nature on the skin of fast swimming sharks (Reif et al. [2].). The drag reduction mechanism can be related to an interaction of riblets with the streaky structures in the viscous sublayer. Riblets oriented into the mean flow direction can hamper the cross flow of the streak structures at the wall. Hence, the vertical motions of the fluid and the turbulent shear stresses are reduced. The streak structures are moved away from the surface and are primarily in contact with the riblet tips.

Idealized geometries with less complexity in comparison to the shark skin were first investigated on flat plates by Walsh [3] at NASA Langley Research Center. Later, in the 1990s, extensive experimental investigations on the effect of various 2D riblet geometries on the skin friction of flat plates were carried out by Bechert et al. [4] in the oil channel of the Institute of Propulsion Technology of the German Aerospace Center (DLR) in Berlin. The experiments were confined to flows with zero pressure gradients. The best drag reduction, up to 10%, was achieved by blade-type ribs. Unfortunately, the structural strength of this type of geometry is expected to be insufficient under operating conditions of aircraft engines or gas turbines. A good compromise between structural strength and drag-reduction potential is achieved, for instance, by riblets with a trapezoidal or triangular groove.

With these types of riblets, a few experiments were carried out by different research groups in order to investigate their potential to reduce profile losses of compressor blades. A brief overview of the results obtained by different research groups is given in Oehlert and Seume [5]. Most of these investigations involved the application of foils carrying small ribs with ideal groove geometries and sharp tips to the surface of the compressor blades. This application technique is neither suitable for industrial nor aircraft gas turbine engine blading, as the foil is expected to be of insufficient mechanical strength under the operating conditions of these engines.

Ideally, the riblets should be manufactured in the bulk material of the turbine or compressor blade on the same machine tool as is used to machine the airfoil shapes of the blade in order to avoid additional setup times. This leads to the main objective, the manufacturing of riblets by means of applicable industrial manufacturing processes, and is the motivation of the research project "riblets for compressor blades" funded by the German Research Foundation (DFG).

As shown by Oehlert and Seume [5] and by Oehlert et al. [6], the initial investigations of riblets created on compressor blades by means of industrial manufacturing processes were very promising. The surface structures were produced on the compressor blades by grinding (IFW) and laser structuring (LZH) as described by Denkena et al. [7] and Siegel et al. [8]. An optimization of the riblet application method by Lietmeyer et al. [9], resulting in an additional reduction of profile loss, involved the adaptation of the riblets to the local flow conditions and the selective placement of the riblets on the blade surfaces.

The present paper presents recent improvements in grinding and laser-structuring techniques for accurate geometric production of riblets on compressor blades and the reduction of production times. Measuring techniques for the evaluation of the geometry of small-scale structures and, finally, a methodology for assessing the aerodynamic impact of riblet geometry on compressor blade profile losses are presented.

Recent Advances in Manufacturing of Riblets by Grinding

Grinding with multiprofiled wheels has been established as an effective method for generating riblet structures on large-scale surfaces. Vitrified bonded grinding wheels can be used to generate microgroove structures with a width of 26 μm to 120 μm (Fig. 1). In order to utilize the full potential of riblet structures with a trapezoidal groove, it is necessary to generate microprofiles with an aspect ratio of riblet height to spacing of $h/s = 0.5$. The ground riblet structures with a spacing of 26 μm, however, did not reach the required aspect ratio and since a riblet spacing as small as 20 μm (with a height of 10 μm) is required for compressor blade applications, the grain size of the abrasive material must be downscaled in order to achieve the required geometries. However, if the grain size is too small, the bonding forces will decrease and the grinding wheel wear will increase (Denkena et al. [7]). In order to reduce tool wear and the dimensional limit inherent in the production of riblet geometries by means of vitrified bonded grinding wheels, metal bonded grinding wheels can be used. Due to the high bonding forces of the metal binding, small grain sizes can be used without an increase of the tool wear (Klocke et al. [10]). In contrast to vitrified bonding, however, metal bonded grinding tools are difficult to dress by conventional dressing methods.

In principle, electronic contact discharge dressing (ECDD) is suitable for generating complex profiles on metal bonded wheels (Denkena et al. [11], Zaeh et al. [12]). Here, one pole of the direct current circuit is connected to an electrode and the other pole is connected to the steel body of the grinding tool by carbon brushes. During dressing chips are generated from the electrode, which establish a distortion of the electric field between the electrode and the metal bond. An arc-over is the result of the increasing field distortion and the chip is vaporized. The thermal energy released in this process melts and removes the bond material locally. The dressing strategy is shown in Fig. 2. The electrode (a copper wire with a diameter of 1 mm) moves radially to the
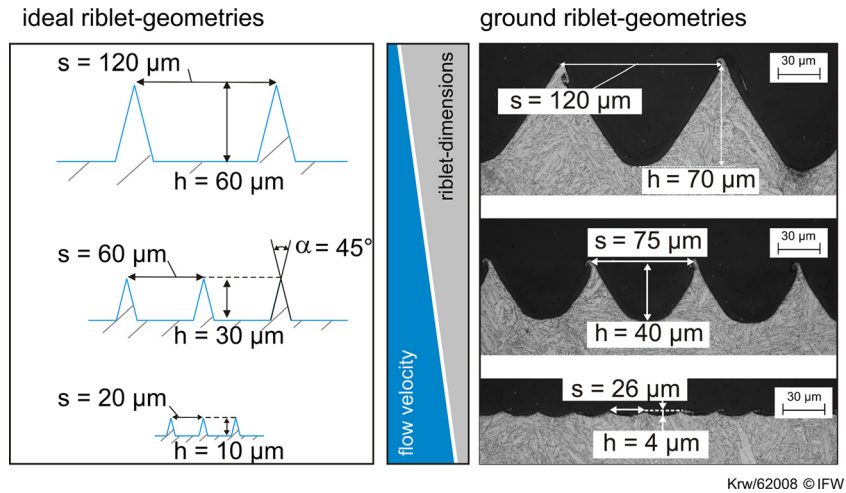
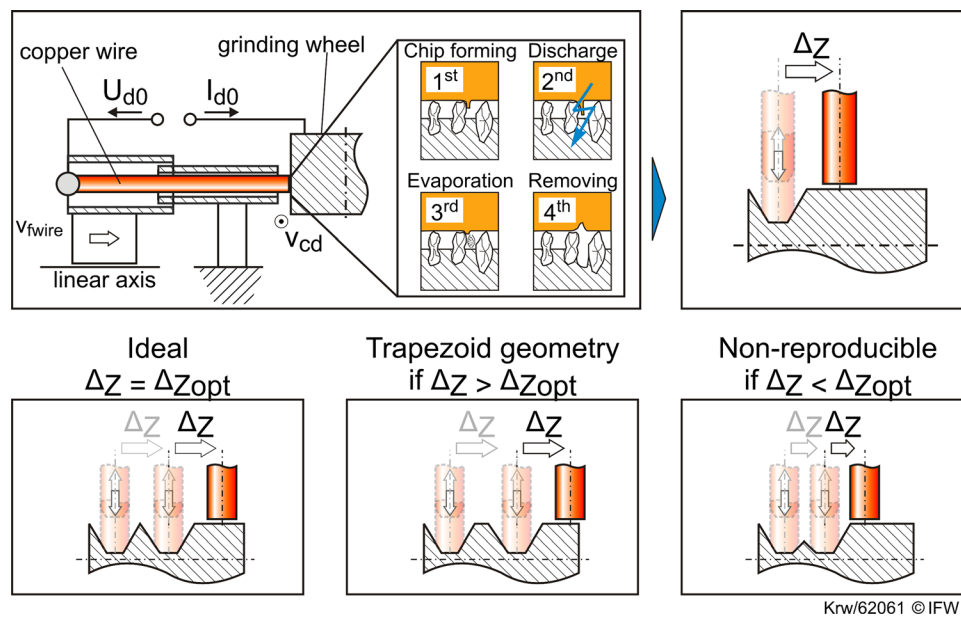**Fig. 1   Riblet geometries ground by vitrified bonded grinding wheels**

Fig. 2   ECDD-strategy

grinding wheel and generates a trapezoidal groove (Fig. 2). In a second step, the wire is displaced about Δz and then moved radially again. Using this strategy, a number of profiles can be created on the grinding wheel. The spacing of the dressed profiles on the grinding wheel is larger than the riblet spacing (Fig. 3). However, a riblet spacing smaller than the profiles on the grinding wheel is generated on compressor blades by a shift strategy (Denkena et al. [7]).

The displacement Δz is varied to find Δz_{opt} which generates the smallest profile geometries on the grinding wheel. The profile geometries, including the profile heights, are evaluated at a profile width of $20\,\mu m$ and $60\,\mu m$ (h_{20} and h_{60}). Trapezoidal profiles will be generated if Δz is too big. In the case of smaller Δz, the height of the microprofiles on the grinding wheel is reduced by an overlap. This means the smallest profiles will be produced if the dressed geometries just touch each other. In this study grinding wheels (MB6.3 and MB10, Fig. 3) with two different grain sizes ($6.3\,\mu m$ and $10\,\mu m$) were utilized. The optimal displacement Δz_{opt} for the grinding wheel MB10 was $1.035\,mm$. The minimum size profiles on grinding wheels with a grain size of $6.3\,\mu m$ were generated at a Δz_{opt} of $1.025\,mm$. The displacement Δz_{opt} is dependent on the grain size due to the dressed groove width. During the

dressing process, the metal bonding melts, grains fall out, and a groove is generated. If a grain with a size of $10\,\mu m$ falls out, the width of the roof will increase about $10\,\mu m$. The increase will be less for smaller grain sizes.

In order to grind riblet structures with a riblet spacing of $20\,\mu m$ and an aspect ratio of $h/s = 0.5$, the grinding wheel profile should have a height h_{20} of nearly $10\,\mu m$. By applying the metal bonded grinding wheel MB10, a profile height of $32\,\mu m$ was reached at a profile width of $60\,\mu m$. A profile height h_{20} could not be measured due to the low sharpness of the profiles. The SEM view shows that there was only one grain on the tip of the grinding wheel profile. As a result, it is not possible to dress smaller profile geometries by applying grinding wheels with a grain size of $10\,\mu m$. Compared to the grinding wheel MB10, the profile height h_{60} of the grinding wheel MB6.3 increased about 100% to $72\,\mu m$. In addition, both results show that the profile geometries were generated with a high reproducibility (Fig. 3). The minimum possible profile geometry is dependent on the grain size due to the fact that at least one grain must be at the peak of the profile. The bigger the grain the bigger the profile geometry. In addition, a great number of grains on the peak of a profile add stability to the peak.
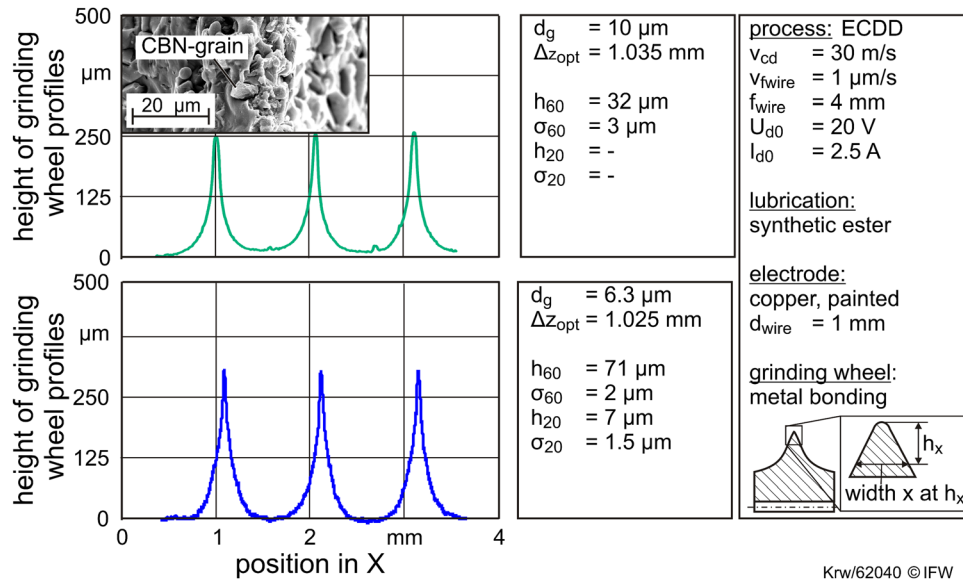
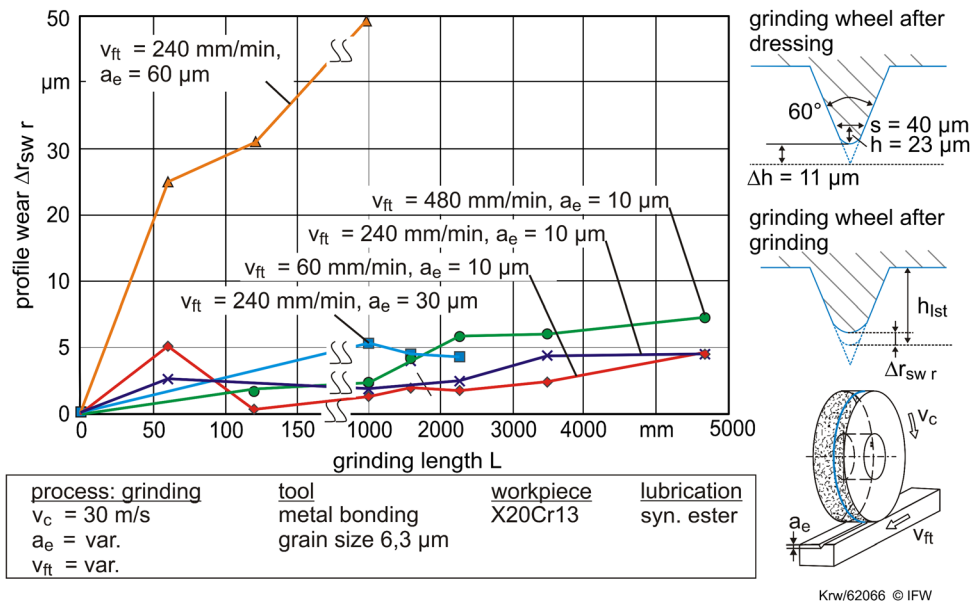Fig. 3   Microprofiles on the grinding wheel

Fig. 4   Wear behavior over the grinding length for different v_f and a_e

ECDD is a time consuming dressing method. In order to dress grooves with a depth of nearly $250\,\mu$m, a copper wire infeed of 4 mm is required. Since the wire moves at a feed rate of $1\,\mu$m per second, 264 min are required to dress three profiles on a grinding wheel. An economical use of metal bonded grinding wheels is possible if the grinding wheels have a low wear rate.

The wear characteristics of metal bonded grinding wheels were, thus, analyzed as part of the present study. The radial wheel profile wear $\Delta r_{sw\ r}$ was evaluated for different depths of cut a_e and feed rates v_{ft} during the grinding of a typical steel material for compressor blades, X20Cr13 (St1.4021). A nearly linear wear behavior across the grinding length L is depicted in Fig. 4. In contrast to the wear of vitrified bonded grinding wheels, metal bonded grinding wheels had a much lower wear rate. A vitrified bonded SiC-grinding wheel at a feed rate of 240 mm/min and a depth of cut of $30\,\mu$m showed a profile wear of $30\,\mu$m after a grinding length of 2000 mm (Klocke et al. [10]). A metal bonded tool had a profile wear of just $5\,\mu$m for the same process parameters.

The variation of the feed rate between 60 mm/min and 480 mm/min at a constant depth of cut had just a minor influence on the profile wear. This behavior suggests that the mechanical loads, which increase with increasing feed rates, do not affect the tool wear. The tool wear is mainly dependent on the depth of cut. At a grinding length of 1000 mm, the radial profile wear at a depth of cut of $60\,\mu$m is much higher than that for a depth of cut of $30\,\mu$m. The increase of the depth of cut raises the contact length between the grinding wheel and the workpiece. A long contact length reduces the supply of lubricant and impedes the removal of chips. The lack of lubricant increases the friction between the grinding wheel and the workpiece. Furthermore, as the chips clog the grinding wheel topography, the grinding effectiveness of the abrasive grains is reduced; thus increasing the thermal loads on the grinding wheel. As a consequence, the thermal loads can increase the profile wear. The supply of lubricant can be improved by using grinding wheels with a larger grain size, but these profiles did not reach the required profile geometries after dressing.
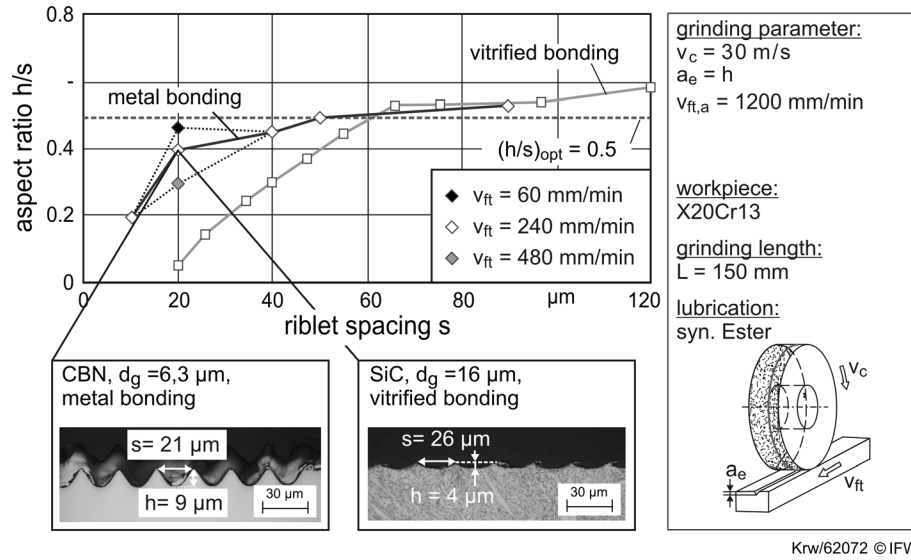
Fig. 5   Aspect ratio of ground riblets

With the metal bonded grinding wheel riblets were generated with a depth of 9 μm and a width of 21 μm and, hence, an aspect ratio of $h/s \approx 0.5$. Such an aspect ratio cannot be attained with vitrified bonded grinding wheels. Nevertheless, the wear of metal bonded grinding wheels at a depth of cut of about 60 μm is unacceptably high (Fig. 5).

Consequently, vitrified and metal bonded grinding wheels have different areas of application. Whereas metal bonded grinding wheels can be used for the manufacturing of small riblet geometries with a riblet height of 10 μm, vitrified bonded grinding wheels should be used for the grinding of riblet structures with a height of more than 30 μm.

Recent Advances in Manufacturing of Riblets by Laser Structuring

As shown in Ref. [6], the production of riblets using short pulsed laser radiation in the pulse length regime of several picoseconds yields very good machining results. The flexibility of laser machining is especially valuable since variable riblet spacing can be easily achieved by simple on-the-fly modification of the machining parameters. A schematic of a laser machining setup is shown in Fig. 6.

Using the shown processing method, an area processing rate of 0.1 mm²/s can be achieved. This speed can be increased significantly by using optical components to split the laser beam into multiples without changing the relevant beam characteristics [13]. Therefore, the available laser power can be fully exploited, whereas with a single beam setup the maximum applicable power is limited by the ablation regime, where pulse energies above 7 μJ–35 μJ cause thermal ablation and insufficient machining results [14]. On modern lasers, pulse energies of 125 μJ are readily available; thus, using an appropriate optical setup, a speed increase up to a factor of 17 is possible depending on the riblet geometry.

Parallel processing is achieved by augmenting the single beam setup with an additional diffractive optical element (DOE) for beam splitting purposes, which is put into the beam between the beam expander and scanner. Since the beam distances in the focal plane are fixed, dynamic rotation of the DOE is used to change the laser spot distance in relation to the scanning direction (Fig. 7).

The fan of laser spots created by the DOE enables the parallel machining of riblets along the entire blade length. This is done by scanning hatched rectangles with a width of the spot-to-spot distance and a hatch distance of the riblet width (Fig. 8). The point-to-point width for every riblet geometry has to be matched for an even overall width to avoid curved outlines that would cause nonmachined areas [15].

So far, an increase in speed by a factor of five was achieved (0.5 mm²/s versus 0.1 mm²/s effective scan speed) using a seven spot DOE. An asymptotical closure by a factor of seven seems highly probable using electro optical switches instead of the mechanical ones used in our experimental setup. The ablation quality is equal to single-spot machining and especially improved
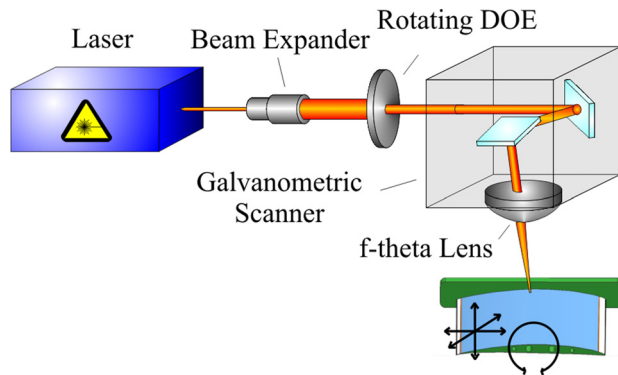

Fig. 6   Principal setup for laser machining. The multiaxis translation system positions the area of interest of the blades into the focal plane of the lens, while the scanner deflects the laser beam at high speed.
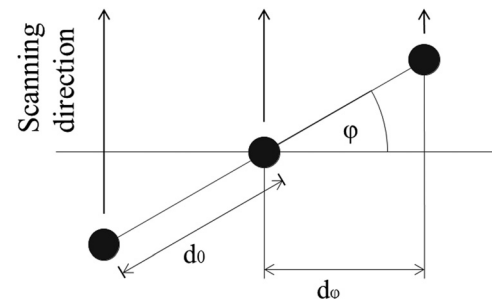

Fig. 7   Principle of three spot ablation using beam splitting DOE; the effective spot-to-spot distance is determined by the rotation angle of the DOE
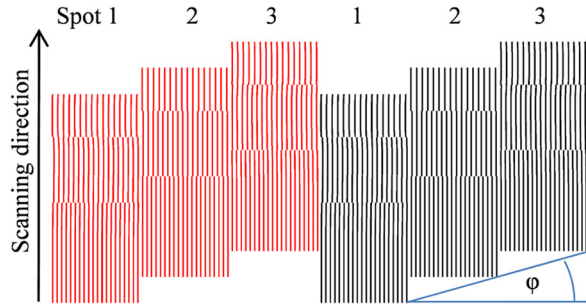
Fig. 8   Simulated lanewise scanning pattern using a three sport DOE: Two lanes are set side by side using three different riblet spacings (from top to bottom).
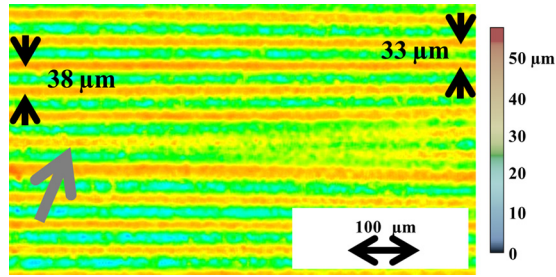

Fig. 9   Magnified confocal microscope image of a smooth parameter set transition from 38 μm to 33 μm riblet spacings. The gray arrow marks a beginning bifurcation.

251 in parameter transition zones, where sudden breaks are smoothed
252 and bifurcations of lower frequency riblets occur (Fig. 9). This
253 brings laser machining of riblets closer to industrial applicability.

254 **Geometrical Measurement of Riblets**

255 **Theory: Physical Limitations of the Measurement Principle.**
256 All optical measurement instruments are characterized by the
257 limited lateral resolution that is often defined as

$$d_{\min} = 0,61 \frac{\lambda}{NA} \qquad (1)$$

258 with the wavelength λ of the used light. Since the numerical aper-
259 ture (NA) of lenses used in air is less than 1, the lateral resolution
260 is limited to approximately 200 nm. Another problem is the lim-
261 ited capability to detect inclined surfaces. The more a surface is
262 tilted, the less light will be reflected into the measurement lens.

Table 1   System characteristics of the confocal microscope

Magnification	20	50	100
Working distance (mm)	3.1	0.66	0.34
Measurement area (μm^2)	800×772	320×308.8	160×154.4
NA	0.46	0.8	0.95
Max. theoretic slope angle (deg)	17.7	26.6	35.5
Lateral resolution (μm)	0.78	0.34	0.2

After reaching the critical angle (approximately 36 deg), the signal 263
becomes too degraded for a reliable surface detection. Undetected 264
points are interpolated to counteract this effect, which sometimes 265
leads to inaccurate results. 266
    Limited adaptability of optic methods is demonstrated in 267
Fig. 10. The intensity distribution of the cutting line is shown in 268
the two image stacks. In the sample processed with the laser (left), 269
the flank is clearly recognizable due to a rough surface. The foil 270
surface (right), in contrast, hardly gives any signal; therefore, only 271
the bottom and the highest points are recognizable. 272
    A μSurf Nanofocus confocal microscope with three objective 273
lenses was used for imaging the riblet structures. The microscope 274
characteristics are summarized in Table 1. 275

Choice of Measurement Lenses. In theory, a lens with 276
$100\times$ magnification is best suited for the measurement. However, 277
$100\times$ lenses have a severe disadvantage: The measurement area is 278
limited to ca. $160 \times 160 \mu$m. As the riblets have a typical spacing 279
of 40–80μm, the measurement only contains 4–2 riblet periods. 280
Such a small area is not suitable for a statistically significant 281
characterization of the riblet-geometry and, therefore, has to be 282
enlarged by capturing the surface in small patches. These patches 283
are normally merged by a correlation method (the so called stitch- 284
ing process). Since the stitching of measured data with many sur- 285
face defects does not always work properly, the $100\times$ lens is not 286
the best solution. A smaller magnification has to be chosen to 287
enlarge the captured area. It was determined experimentally that 288
the use of the $20\times$ lens results in errors in the detection of the tip 289
radii due to poor lateral resolution and the riblet profile was not 290
reproduced accurately due to optical artifacts such as bat-wings. 291
Therefore, the use of the $20\times$ lens is not recommended for riblet 292
analysis. The $50\times$ lens was chosen because it provides the best 293
compromise between lateral resolution and measurement area 294
even though the measurement results differ from those obtained 295
using the $100\times$ lens, which shows slightly more accurate results 296
because of the higher lateral resolution. This effect is also 297
depicted in the histograms (Fig. 14). 298

Interpolation of Surface Defects. Due to the steep flank angle 299
of the riblet structures, the information in the area of the flanks 300
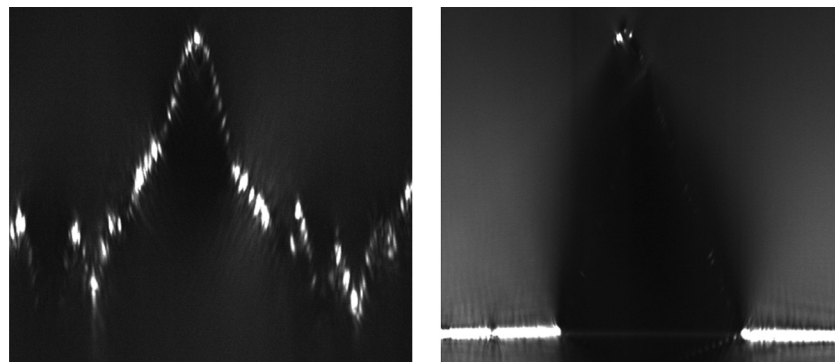

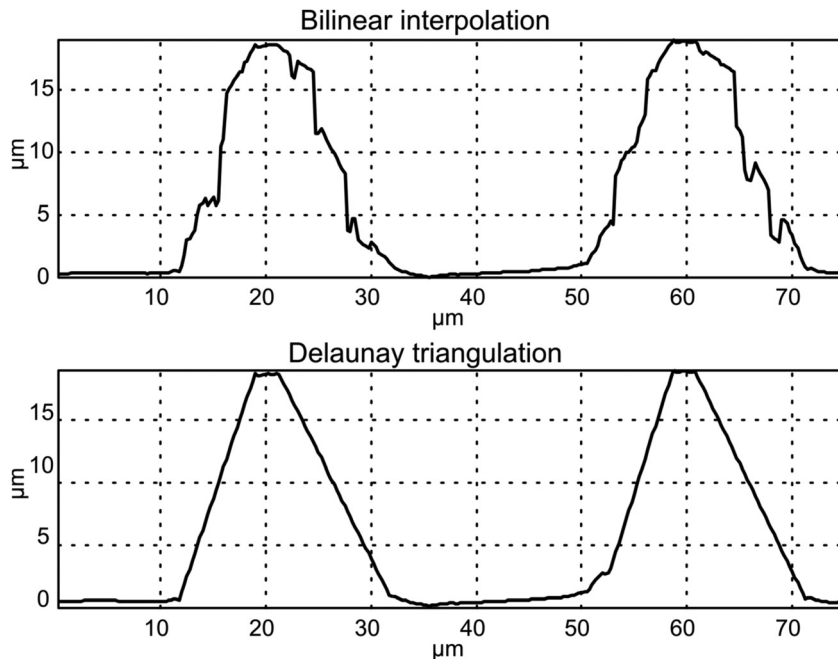**Fig. 10   Intensity distribution through the image stack for different samples**

Fig. 11   Results of bilinear interpolation (top) and interpolation based on Delaunay triangulation

must be estimated by interpolation. Typically, bilinear interpolation is utilized, but investigations of nearly ideal riblet structures (especially when using lenses with $50\times$ and $100\times$ magnification) indicated that bilinear interpolation results in a significantly inaccurate indication of surface deformation (Fig. 11). Hence, the triangle-based cubic interpolation was used instead of the bilinear interpolation. The basic triangles are defined with the help of Delaunay triangulation. A result of the interpolation is depicted in Fig. 11.

Calculation of Main Parameters. The aerodynamic performance of the riblets is a function of their spacing, height and tip radius. These parameters are measured using the following methodology.

Riblet Spacing and Height. The spacing of the riblets produced by grinding and laser structuring varies over the surface. In order to define this variation, the calculation of the riblet spacing is performed locally over a small region within the overall measured area. This region is moved along the whole surface, and at each position, the significant parameters are calculated as shown in step two.

(1) Region preprocessing. The region described in step 1 has to be large enough to contain at least two complete riblet periods. Since the riblets are periodic structures, they can be approximated with dominant and harmonic waves using fast Fourier transformation (FFT). In order to obtain correct results from the FFT, the examined region has to contain whole-numbered amounts of riblet waves. If the requirements are not met, the so-called leakage effect will occur and the structures are approximated by waves of incorrect frequencies. Because the period length is not known a priori, this condition is not met generally, and therefore, the region will be cut out using zero-padding technique (Vynnyk [16]).

(2) Region analysis. The following steps are performed after preprocessing the selected region as described in step 1:

(a) FFT for preprocessed region
(b) Simplification of the spectrum (all frequencies except the dominant wave and their three harmonics are set to zero)
(c) Inverse FFT.

A result of such "simplification" of a complex manufactured surface structure is shown in Fig. 12.

Tip Radii. Contrary to the spacing and height of the riblets, the tip radii are not integral characteristics, but describe a local behavior of the surface. Therefore, the FFT cannot be applied to evaluate the tip radii and the following steps should be performed:

(1) One period is extracted using the region analysis.
(2) The upper 5% of the profile data is cut off from the rest. These data describe the actual tip area of the riblet as shown in Fig. 13.
(3) A third order polynomial fit is performed from which the peak point is obtained.
(4) If the radius of curvature at the peak of the third order polynomial fit obtained in step 3 is less than the width of the 5% "profile tip" obtained in step 2, it is assumed to be the riblet tip radius.

Verification of the Tip Radii With the SEM. As shown in the histograms (Fig. 14), the calculated tip radii depend on the lens used for making the measurements. In order to clear the impreciseness, a scanning electron microscope (DSM 940 A) with a two detector system and an image–acquisition unit from Point Electronics was used to verify the riblet tip radii.

A typical SEM-picture of a foil sample is shown in Fig. 15. The bright areas represent the riblet flanks, whereas the dark areas denote the horizontal areas. A cut through the picture gives a profile as seen in Fig. 15.

The tip width can be considered to be the distance between the highest negative and positive inclination of the intensity distribution. The flank angle should also be accounted for in the calculation of the tip radius. However, in order to maintain compatibility with the optical measured data, the influence of the flank angle is neglected and the tip radius is defined as follows:

$$r = t/2 \qquad (2)$$

The SEM measurements of the tip radius correspond to the measurements made with the confocal microscope and the $50\times$ magnification lens within 20% in all cases.
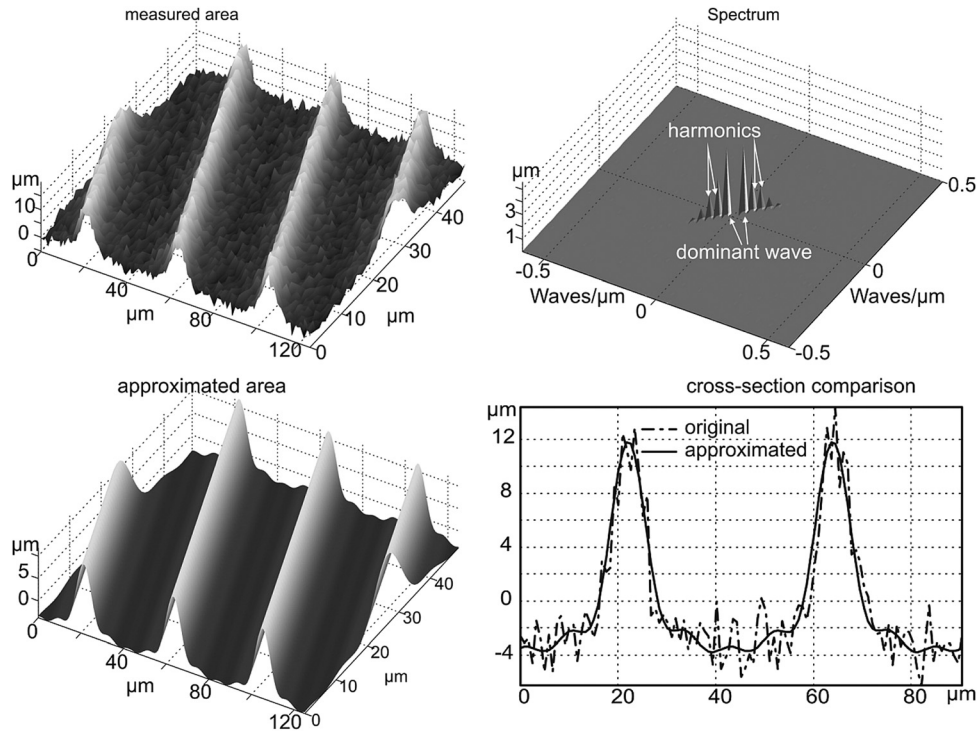
measured area

Spectrum

Fig. 12   Elimination of the stochastic parts

riblets cross section

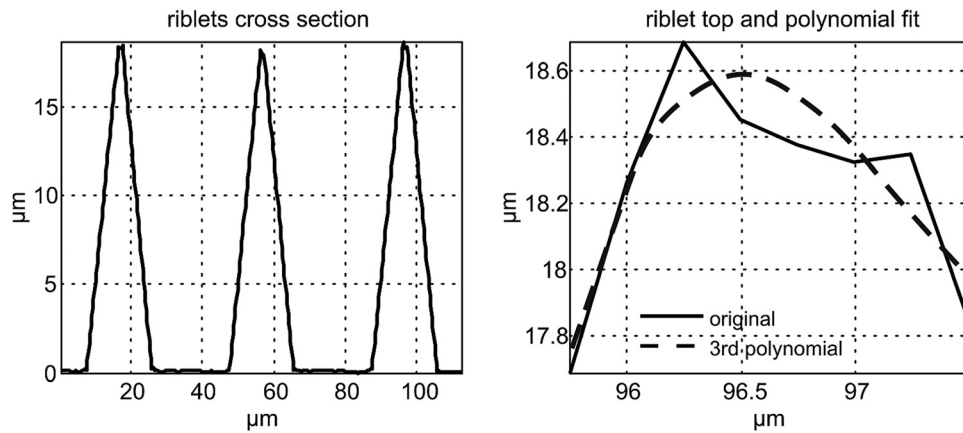riblet top and polynomial fit

Fig. 13   Definition of the top area

Tip radii of measured surface measured with
100x lens. Mean=0.24 μm, Std. Dev.=0.07 μm

Tip radii of measured surface measured with
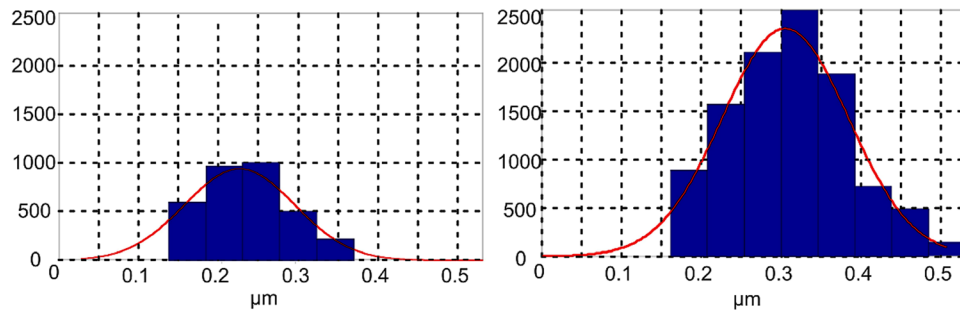50x lens. Mean=0.30 μm, Std. Dev.=0.08 μm

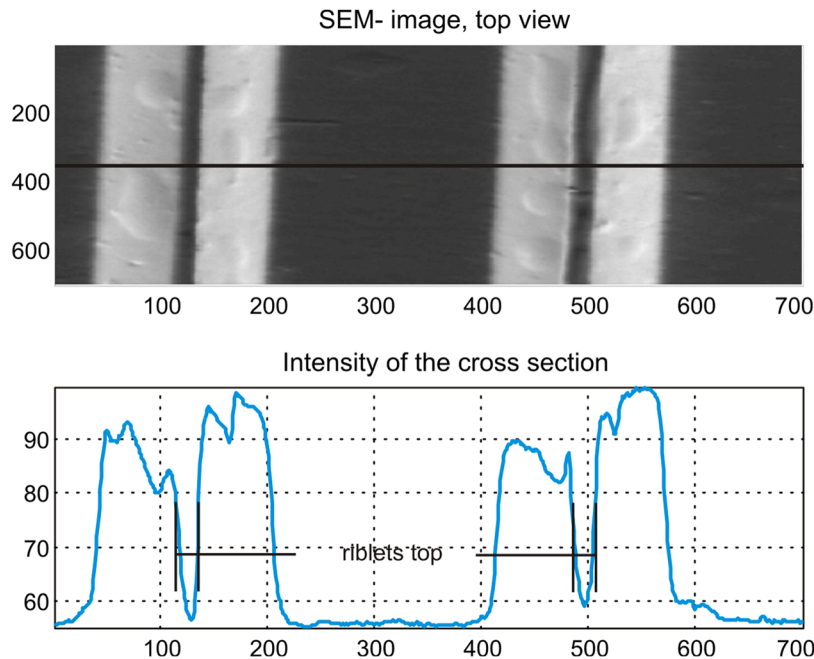**Fig. 14   Different measurement results of the same specimen**

Fig. 15   Evaluation of the riblets radii using SEM

Aerodynamic Measurements

Wall Shear-Stress Reduction. Investigations to validate the aerodynamic effectiveness of ribs manufactured by grinding and laser structuring were carried out under ideal flow conditions in the oil channel at the Institute of Propulsion Technology of the DLR in Berlin. The main advantage of these investigations; in contrast to the investigations conducted on compressor blades in the linear cascade wind tunnel, is that the effect of the surface structures on skin friction was determined under the simplest flow conditions, using flat plates with the riblets perfectly aligned with

the main flow direction under a zero pressure gradient. Prior to the investigations in the oil channel, ribs were manufactured by grinding and laser structuring on X20Cr13 probe material in small scales, comparable to the size of the ribs suitable for application on compressor blades. Subsequently, the geometry of the manufactured microstructures was measured using the optical measuring techniques described above. After postprocessing the measured data, the surface structures were scaled up to maintain Reynolds similarity for the measurements in oil. The scaled up riblet geometries were generated on the flat plates by rapid prototyping as described in Oehlert at al [6]. More information on the oil channel test facility and the measurement setup is given in Bechert et al. [4].

Experimental results showing the influence of ground and laser-structured ribs on the relative change of wall shear-stress $\Delta\tau/\tau_0$ as a function of the dimensionless riblet-spacing s^+ in comparison to riblets with an ideal trapezoidal and triangular groove geometry obtained by Bechert et al. [4] are given in Fig. 16. The chosen target riblet geometry, characterized by a trapezoidal groove with a flank opening-angle at the tip of $\alpha = 30$ deg and a riblet height to spacing ratio of $h/s = 0.5$, is compared to the ground and laser-structured ribs of the present investigation in Fig. 17. The geometrical parameters in the evaluation of the aerodynamic effectiveness of the riblets are given in Table 2. In addition to h/s and the ratio of riblet tip diameter to riblet spacing t/s, a shape factor X is introduced to describe the triangular or the trapezoidal similarity of the groove:

$$X = \frac{A - A_{\text{triangular}}}{A_{\text{trapezoidal}} - A_{\text{triangular}}} \qquad (3)$$

For $X = 0$, the shape of the groove is an ideal triangle. For $X = 1$ the groove has an ideal trapezoidal shape. The shape factor is calculated by the IMR during the postprocessing of the optical measurement data.   AQ5

An additional increase of wall shear-stress reduction of $\Delta\tau/\tau_0 = -1\%$ is the result of improvements in the manufacturing techniques as is demonstrated by a comparison of the data presented by Oehlert et al. [6] with the result of the present investigations in Fig. 16. According to Table 2, this enhancement is
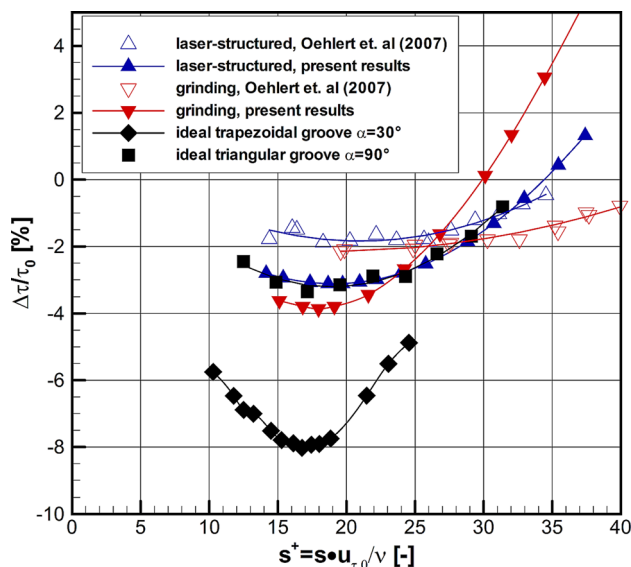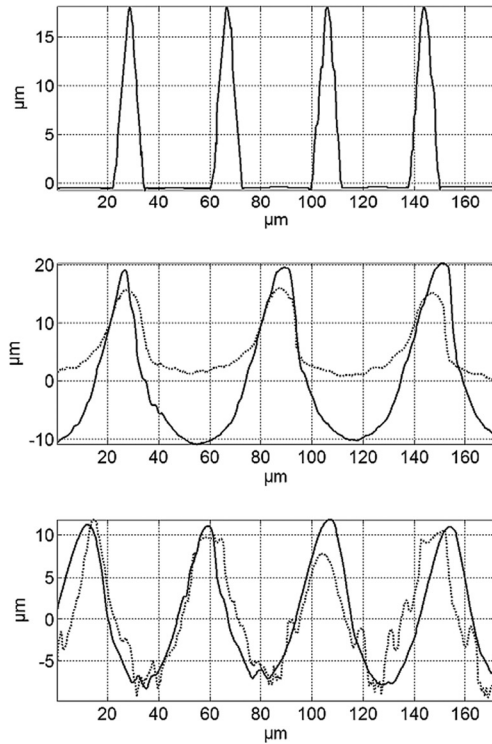

Fig. 16 Wall shear-stress reduction of ground and laser-structured riblets in comparison to riblets with an ideal shape (experimental data measured by the German Aerospace Center, Institute of Propulsion Technology, Engine Acoustics Department); curves obtained by polynomial interpolation; $\sigma = \pm 0.3\%$

Fig. 17   Representative cross sections of ground and laser-structured riblets in comparison to the ideal geometry with a trapezoidal groove

Table 2   Geometric parameters of ground and laser-structured ribs

Riblets	h/s	t/s	X (%)
Laser-structured [6]	0.39	0.04	10.2
Laser-structured, present results	0.39	0.04	32.5
grinding [6]	0.25	0.04	51.4
Grinding, present results	0.49	0.02	53.1

AQ4

Fig. 18   Comparison of measured and calculated wall shear-stress reduction for ideal riblet; error bars indicate the standard deviation σ

primarily due to a nearly optimal h/s of the ground ribs and an increasingly sharp riblet tip. For the laser-structured ribs, this enhancement can be related to the more trapezoidal groove geometry. Further improvements towards reducing skin friction can, thus, be achieved by an additional decrease of the tip diameter and a more trapezoidal shape of the groove geometry to even further dampen the cross flow of the streak structures at the wall.

Calculation of Wall Shear-Stress Reduction. An empirical model was developed to investigate the potential for the optimization of the grinding and laser-structuring processes. The model enables the calculation of the wall shear-stress reduction $\Delta\tau/\tau_0$ of riblets as a function of the geometrical riblet-parameters spacing s, height h, tip-radius r, and shape factor X. The model was derived by a regression analysis of the oil channel data obtained for ideal riblets by Bechert et al. [4] and Hage and Bechert [17], as well as various riblets produced by grinding and laser structuring.

Exemplary comparisons between calculated and measured wall shear-stress reduction $\Delta\tau/\tau_0$ as a function of the dimensionless riblet spacing s^+ for ideal structures and for ground and laser-structured riblets are given in Figs. 18 and 19.

In order to take into account the stochastic distributions of the ground and laser-structured ribs, probabilistic simulations were carried out using a Monte Carlo simulation (MCS). A Latin hypercube sampling (LHS) was applied to take random samples from the probability density functions of the rib geometry parameters as depicted in Fig. 20. Overall, $N = 2000$ samples were taken for the MCS. It was determined in preliminary investigations that the mean values and standard deviations of the results are independent of the sample number for $N = 2000$. Extensive calculations to validate the model, which are not shown here, were conducted on different rib structures produced by grinding and laser structuring. Overall, the experimental and calculated wall shear-stress reduction corresponds well and the validation process showed that the physical effects of the geometry parameters on wall shear-stress are well captured by the model.
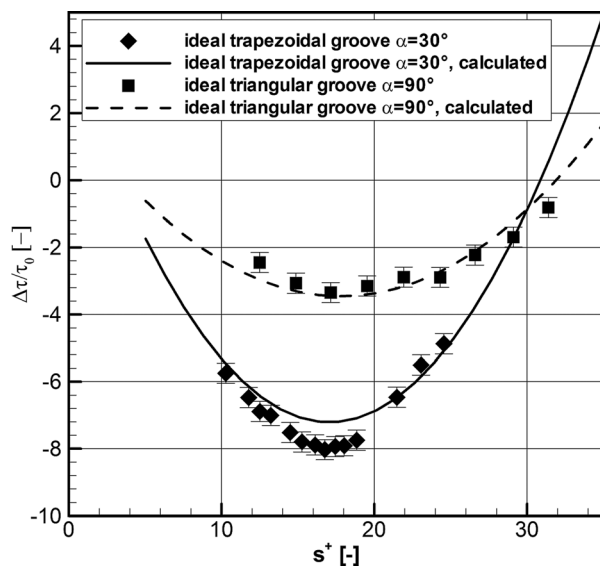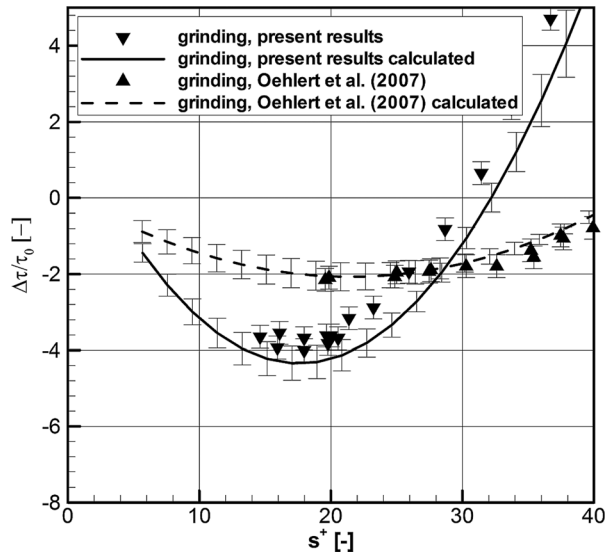
Fig. 19 Comparison of measured and calculated wall shear-stress reduction for ground and laser-structured riblets; error bars indicate the standard deviation σ
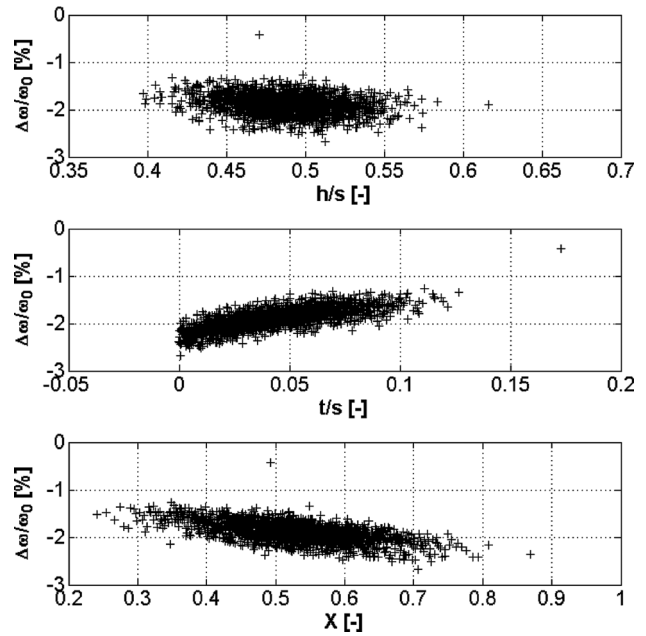

Fig. 21   Anthill plots of profile-loss reduction

Probabilistic Calculations on Compressor Blades.   Numerical calculations on riblet-structured NACA 6510 compressor blades were performed using MISES, which is a viscous-inviscid cascade analysis and design system. A brief overview of the cascade flow solution method used in MISES is given by Drela and Giles [18]. MISES was modified and validated in order to account for the drag-influencing effects of ideal trapezoidal groove riblets by Lietmeyer et al. [19]. To evaluate the drag-influencing effects of ground and laser-structured riblets, the model of shear-stress reduction as an empirical function of the riblet geometry described above was implemented in MISES.

Numerical simulations using MISES embedded in a Monte Carlo simulation were performed in order to calculate the profile-loss reduction of a blade structured by grinding. The goal of the simulations was to define further improvements in the structuring process. For the Latin hypercube sampling, the probability density functions of the geometrical parameters of the surface structure were taken into account as shown in Fig. 20. The blade was structured only on the suction side in the turbulent boundary layer downstream of a dimensionless chord length of $x/c = 0.4$. Overall, $N = 2000$ simulations were conducted using MISES. For each simulation run, the pressure loss coefficient was calculated:

$$\omega = \frac{p_{\text{tot},1} - p_{\text{tot},2}}{p_{\text{tot},1} - p_{\text{stat},1}} \qquad (4)$$

To determine the effect of the riblets on the pressure loss, the difference in the loss coefficient was calculated:

$$\frac{\Delta\omega}{\omega_0} = \frac{\omega - \omega_0}{\omega_0} \qquad (5)$$
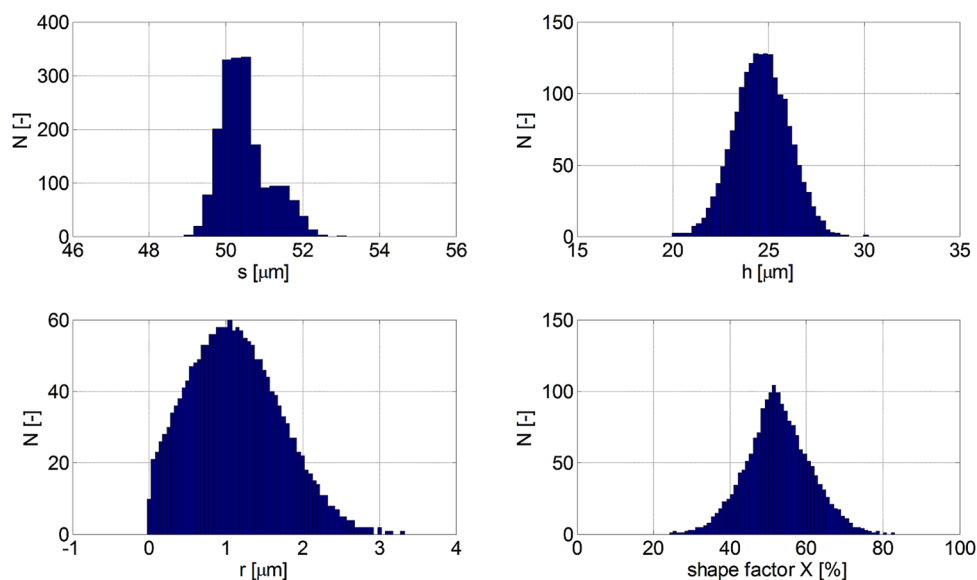

Fig. 20   Probability density functions of geometric parameters of a ground riblet structure on a NACA 6510 compressor blade (measured by IMR)
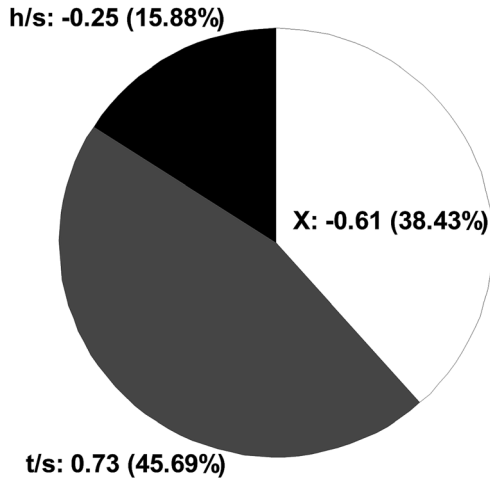
Fig. 22   Pie chart of profile-loss reduction

479 In Eq. (5) ω is the loss coefficient of the riblet-structured blade
480 and ω_0 is the loss coefficient of the smooth reference blade. The
481 cascade inlet flow conditions are M = 0.5 and Re = 10^6. Further
482 information on the experimental setup and blade specifications is
483 given in Ref. [9].
484 As a result of the MCS with MISES, a mean profile-loss reduc-
485 tion of $\Delta w/w_0 = -1.89\% \pm 0.42\%$ was calculated for the current
486 blade structured by grinding and is in good accordance with the
487 experimental result of $\Delta w/w_0 = -1.38\% \pm 0.29\%$. Additional
488 conclusions from the numerical results can be drawn by plotting
489 the profile-loss reduction ω/ω_0 over each individual realization of
490 the MCS as depicted in Fig. 21. By applying a correlation analysis
491 of the data, Pearson's correlation coefficient was calculated.
492 Results of the correlation analysis are plotted in a pie-chart
493 by normalizing each correlation coefficient by the total sum
494 (Fig. 22). With the help of this analysis it becomes obvious that an
495 additional reduction of profile loss can be achieved by decreasing
496 the riblet tip diameter and by a more trapezoidal shaped groove.
497 This supports the experimental results obtained in the oil channel
498 presented above.

499 ## Conclusions

500 Recent advances in the manufacturing of riblets by grinding
501 and laser structuring in relation to the geometric quality of the ribs
502 and their aerodynamic effectiveness are presented.
503 Grinding with multiprofiled grinding wheels is an effective
504 method for generating riblets on large-scale surfaces. With vitri-
505 fied bonded grinding wheels, a reproducible aspect ratio of riblet
506 height to spacing of $h/s = 0.5$ is presently only achievable for a
507 riblet spacing of $s > 60\,\mu m$. This is the optimal aspect ratio for
508 attaining the maximum reduction of skin friction for riblets with a
509 trapezoidal groove, which is the target geometry. However, espe-
510 cially near the leading edge of compressor blades under turboma-
511 chinerylike flow conditions, the desired riblet spacing is $s < 60\,\mu m$
512 with a minimum of $s \approx 20\,\mu m$. To achieve the aspect ratio of
513 $h/s = 0.5$ for such small riblet spacings, metal bonded grinding
514 wheels were applied due to their smaller grain size. With metal
515 bonded grinding wheels, riblets with a spacing of $s > 17\,\mu m$ and
516 an aspect ratio of $h/s = 0.4$ were achieved, which is a significant
517 improvement compared to vitrified bonded grinding wheels. A
518 promising result is a reduction in the wear of metal bonded grind-
519 ing wheels to 1/6 of the wear of vitrified bonded grinding wheels
520 for a cut depth smaller than $30\,\mu m$. For a cut depth greater than
521 $30\,\mu m$, the wear of metal bonded grinding wheels significantly
522 increases. This leads to the conclusion that grinding wheels with a
523 metal bonding are particularly suitable for the manufacturing of

524 small riblet geometries with a riblet height of 10 to $30\,\mu m$. Vitri-
525 fied bonded grinding wheels should be applied for the grinding of
526 riblet structures with a riblet height of more than $30\,\mu m$.
527 For the laser-structuring process, a significant decrease of
528 production time was achieved by applying diffractive optical ele-
529 ments. Presently, an increase in speed by a factor of five has been
530 achieved using a seven-spot DOE. The variation of the rotation
531 angle of the DOE during the manufacturing process provides the
532 opportunity for a continuous adaption of the riblet geometry along
533 the blade's surface to the local flow conditions.
534 To characterize the aerodynamic impact of the riblets manufac-
535 tured by grinding and laser-structuring, the surface structures
536 were measured with a confocal microscope and 50 times magnifi-
537 cation. The measured values were confirmed with a scanning elec-
538 tron microscope. The structured surface was measured in small
539 patches that were stitched together in the postprocessing. Proba-
540 bility density functions of riblet spacing and height were calcu-
541 lated by an FFT. The probability density function of the riblet tip
542 diameter was calculated by means of a third order polynomial
543 approximation.
544 For both ground and laser-structured ribs, an additional reduc-
545 tion of wall shear-stress by approximately $\Delta\tau/\tau_0 = -1\%$ was
546 obtained due to improvements in the manufacturing techniques,
547 which presently leads to a maximum reduction in skin friction of
548 $(\Delta\tau/\tau_0)_{max} \approx -4\%$. For the ground ribs, this enhancement is
549 shown to be primarily due to a nearly optimal riblet height-to-
550 spacing ratio and sharper riblet tips. For the laser-structured ribs,
551 this enhancement can be related to the more trapezoidal groove
552 geometry. A further reduction of skin friction could, thus, be
553 achieved by a further decrease of the tip diameter and a more trap-
554 ezoidal shape of the groove geometry.
555 To assess the impact on compressor blade profile losses and in
556 order to indentify the potential for future optimization of the
557 grinding and laser-structuring processes, an empirical model of
558 wall shear-stress reduction as a function of the relevant riblet
559 geometry parameters was developed. The empirical model was
560 implemented in the viscous-inviscid cascade analysis code
561 MISES. This combination delivers a design tool to calculate pro-
562 file losses of riblet-structured linear blade cascades. Numerical
563 simulations with MISES embedded in a Monte Carlo simulation
564 (MCS) were performed in order to calculate the profile-loss
565 reduction of a compressor blade structured by grinding. As a
566 result of the MCS with MISES, a mean profile-loss reduction of
567 $\Delta w/w_0 = -1.89\% \pm 0.42\%$ was calculated and is in good accord-
568 ance with the experimental result of $\Delta w/w_0 = -1.38\% \pm 0.29\%$.
569 By applying a correlation analysis of the data obtained by the
570 MCS and a calculation of Pearson's correlation coefficient, it was
571 confirmed that an additional reduction of profile loss of up to 4%
572 for the investigated NACA 6510 compressor cascade can be
573 achieved by decreasing the riblet tip diameter further and by a
574 more trapezoidal shaped groove. This loss reduction was meas-
575 ured by Ref. [9] on the compressor cascade carrying a riblet foil
576 on the suction side with an ideal trapezoidal groove geometry.

Nomenclature

A = cross-sectional area (μm^2)
a_e = cut depth (μm)
c = chord length (mm)
d = diameter (μm)
d_g = grain size (μm)
d_{min} = limited lateral resolution (nm)
d_{wire} = diameter of the copper wire (mm)
d_0 = beam distance in focal plane (μm)
d_φ = beam distance in relation to scanning direction (μm)
f_{wire} = infeed of the wire (mm)
h = riblet height (μm)
h_{20} = profile height at a width of 20 μm (μm)
h_{60} = profile height at a width of 60 μm (μm)
I_{d0} = short circuit current (A)
L = grinding length (mm)
M - = Mach number
N = number of observations
NA = numerical aperture
p = pressure (Pa)
r = riblet tip-radius (μm)
Re = Reynolds number
s = riblet spacing (μm)
t = riblet tip-diameter (μm)
u_τ = (skin) friction velocity (m/s)
v_c = cutting speed (m/s)
v_{cd} = cutting speed at dressing (m/s)
v_{ft} = feed rate (mm/min)
v_{fwire} = feed rate of the wire (μm/s)
x, y, z = wall coordinates (mm)
X = riblet groove shape factor
$\Delta r_{sw\,r}$ = radial wheel profile wear (μm)
Δz = lateral displacement (mm)

Greek Symbols

α = flank opening-angle at the riblet tip (deg)
φ = rotation angle (deg)
σ = standard deviation
τ = wall shear-stress (N/m^2)
λ = wavelength (nm)
ω = pressure loss coefficient

Subscripts

opt = optimal
tot = total
stat = static
0 = reference
+ = nondimensional, in wall coordinates

Abbreviations

DLR = German Aerospace Center
ECDD = electronic contact discharge dressing
IFW = Institute of Production Engineering and Machine Tools
IMR = Institute for Measurement and Automatic Control
LZH = Laser-Center Hannover
NASA = National Aeronautics and Space Administration
SEM = scanning electron microscope
TFD = Institute of Turbomachinery and Fluid Dynamics

References

[1] Gümmer, V., (2005), "Pfeilung und V-Stellung zur Beeinflussung der Dreidimensionalen Strömung in Leiträdern Transsonischer Axialverdichter, "Fortschritt-Berichte VDI Reihe 7 Nr. 384, VDI Verlag, Düsseldorf.

[2] Reif, W.-E., 1985, "Squamation and Ecology of Sharks," Courier Forschungsinstitut Senckenberg, Frankfurt/Main, **78**.

[3] Walsh, M. J., 1983, "Turbulent Boundary Layer Drag Reduction Using Riblets," AIAA paper 82-0169.

[4] Bechert, D. W., Bruse, M., Hage, W., van der Hoeven, J. G. T., and Hoppe, G., 1997, "Experiments on Drag-Reducing Surfaces and Their Optimization With an Adjustable Geometry," J. Fluid Mech., **338**, pp. 59–87.

[5] Oehlert, K., and Seume, J., 2006, "Exploratory Experiments on Machined Riblets on Compressor Blades," Proc. of Fluids Engineering Division Summer Meeting 2006, Miami, FL, FEDSM 2006 – 98093.

[6] Oehlert, K. Seume, J. Siegel, F. Ostendorf, A. Wang, B.; Denkena, B. Vynnyk, T. Reithmeier, E. Hage, W. Knobloch, K., and Meyer, R., 2007, "Exploratory Experiments on Machined Riblets for 2-D Compressor Blades," Proceedings of International Mechanical Engineering Conference and Exposition 2007, Seattle, WA, IMECE 2007 – 43457.

[7] Denkena, B., Koehler, J., and Wang, B., 2010, "Manufacturing of Functional Riblet Structures by Profile Grinding," CIRP J. Man. Sci. Tech., **3**, pp. 14–26.

[8] Siegel, F., Klug, U., and Kling, R., 2009, "Extensive Micro-Structuring of Metals Using Picosecond Pulses—Ablation Behavior and Industrial Relevance," J. Laser Micro. Nanoeng., **4**, pp. 104–110.

[9] Lietmeyer, C., Oehlert, K., and Seume J. R., 2011, "Optimal Application of Riblets on Compressor Blades and Their Contamination Behaviour," Proceedings of ASME Turbo Expo 2011, Vancouver, Canada, GT2011-46855.

[10] Klocke, F., Klink, A., and Schneider, U, 2007, "Electrochemical Oxidation Analysis for Dressing Bronze-Bonded Diamond Grinding Wheels," Prod. Engineer., **1**(2), pp. 141–148.

[11] Denkena, B., Reichstein, M., and Hahmann, D., 2006, "Electro Contact Discharge Dressing for Micro-Grinding," Proceedings of the 6th euspen International Conference, Baden, Austria, pp. 92–956.

[12] Zaeh, M. F., Brinksmeier, E., Heinzel, C., Huntemann, J. W., and Föckerer, T, 2009, "Experimental and Numerical Identification of Process Parameters of Grind-Hardening and Resulting Part Distortions," Prod. Engineer., **3**(3), pp. 271–279.

[13] Golub, M., 2004, "Laser Beam Splitting by Diffractive Optics," Opt. Photonics, **15**(2).

[14] Siegel, F., 2011, "Abtragen metallischer Werkstoffe mit Pikosekunden-Laserpulsen für Anwendungen in der Strömungsmechanik," Dissertation, Berichte aus dem LZH, Band 02/2011.

[15] Wojakowski, B., Klug, U., and Kling, R., 2011, "Large-Area Production of Dynamically Scaled Microstructures Using Diffractive Optical Elements," Proceedings of International Congress on Applications of Lasers and Electro-Optics (ICALEO) 2011, Orlando, FL, M603.

[16] Vynnyk, T., 2010, "REM-Topografiemessungen an Mikro- und Nanostrukturierten Oberflächen," Dissertation, Leibniz Universität Hannover.

[17] Hage, W., and Bechert, D. W., 2001, "Rib Tip Sharpness: A Key Issue for Riblet Application," Interner Bericht, DLR-IB 92517-01/B7.

[18] Drela, M., and Giles, M. B., 1987, "Viscous-Inviscid Analysis of Transonic and Low Reynolds Number Airfoils," AIAA J., **25**(10), pp. 1347–1355.

[19] Lietmeyer, C., Chahine, C., and Seume, J. R., 2011, "Numerical Calculation of the Riblet-Effect on Compressor Blades and Validation with Experimental Results," Proceedings of IGTC 2011, Osaka, Japan, IGTC2011-0106.

AQ6

AQ7

AQ8

AQ9

AQ10

AQ11